



This is a repository copy of *Quantifying atrial anatomy uncertainty from clinical data and its impact on electro-physiology simulation predictions*.

White Rose Research Online URL for this paper:  
<http://eprints.whiterose.ac.uk/154452/>

Version: Published Version

---

**Article:**

Corrado, C., Razeghi, O., Roney, C. et al. (8 more authors) (2020) Quantifying atrial anatomy uncertainty from clinical data and its impact on electro-physiology simulation predictions. *Medical Image Analysis*, 61. 101626. ISSN 1361-8415

<https://doi.org/10.1016/j.media.2019.101626>

---

**Reuse**

This article is distributed under the terms of the Creative Commons Attribution (CC BY) licence. This licence allows you to distribute, remix, tweak, and build upon the work, even commercially, as long as you credit the authors for the original work. More information and the full terms of the licence here:  
<https://creativecommons.org/licenses/>

**Takedown**

If you consider content in White Rose Research Online to be in breach of UK law, please notify us by emailing [eprints@whiterose.ac.uk](mailto:eprints@whiterose.ac.uk) including the URL of the record and the reason for the withdrawal request.



[eprints@whiterose.ac.uk](mailto:eprints@whiterose.ac.uk)  
<https://eprints.whiterose.ac.uk/>



# Quantifying atrial anatomy uncertainty from clinical data and its impact on electro-physiology simulation predictions

Cesare Corrado<sup>a,\*</sup>, Orod Razeghi<sup>a</sup>, Caroline Roney<sup>a</sup>, Sam Coveney<sup>b</sup>, Steven Williams<sup>a</sup>, Iain Sim<sup>a</sup>, Mark O'Neill<sup>a</sup>, Richard Wilkinson<sup>c</sup>, Jeremy Oakley<sup>c</sup>, Richard H. Clayton<sup>b</sup>, Steven Niederer<sup>a</sup>

<sup>a</sup> Division of Imaging Sciences & Biomedical Engineering, King's College London, London SE17EH, United Kingdom

<sup>b</sup> Insigneo Institute for in-silico Medicine and Department of Computer Science, University of Sheffield, Sheffield, United Kingdom

<sup>c</sup> School of Mathematics and Statistics, University of Sheffield, Sheffield, United Kingdom

## ARTICLE INFO

### Article history:

Received 31 May 2019

Revised 5 November 2019

Accepted 5 December 2019

Available online 12 December 2019

### Keywords:

Uncertainty quantification

Cardiac models

Principal component analysis

Medical image processing

## ABSTRACT

Patient-specific computational models of structure and function are increasingly being used to diagnose disease and predict how a patient will respond to therapy. Models of anatomy are often derived after segmentation of clinical images or from mapping systems which are affected by image artefacts, resolution and contrast. Quantifying the impact of uncertain anatomy on model predictions is important, as models are increasingly used in clinical practice where decisions need to be made regardless of image quality. We use a Bayesian probabilistic approach to estimate the anatomy and to quantify the uncertainty about the shape of the left atrium derived from Cardiac Magnetic Resonance images. We show that we can quantify uncertain shape, encode uncertainty about the left atrial shape due to imaging artefacts, and quantify the effect of uncertain shape on simulations of left atrial activation times.

© 2019 The Authors. Published by Elsevier B.V.

This is an open access article under the CC BY license. (<http://creativecommons.org/licenses/by/4.0/>)

## 1. Introduction

Patient-specific models of the heart are increasingly used to diagnose and treat patients (Niederer et al., 2019; Colli Franzone et al., 2006). Personalised cardiac models are routinely developed from clinical images. Segmentation of these images defines the cardiac anatomy, and meshing these segmentations provides a mathematical description of the shape of the heart. The equations describing cardiac function can then be solved over the mesh to predict the response to the treatment.

If cardiac models are to be used routinely in the clinic it will be increasingly important to understand the effects of data uncertainty on model predictions, as well as what level of data quality is required to make models with sufficient accuracy to inform patient care (Mirams et al., 2016; Gray and Pathmanathan, 2018). Recent studies have considered the impact of uncertainty in determining local tissue excitability (Dhamala et al., 2018), in the activation map in the presence of an uncertain conductivity tensor (Quaglino et al., 2018), and on the distribution of the epicardial extra-cellular potential including the ST duration

(Johnston et al., 2018). However, the effect of uncertainty in model shape on simulation predictions has not been addressed.

Clinical images of the heart from echocardiography, computed tomography scans (CT), magnetic resonance imaging (MRI) or patient anatomies recorded using electro-anatomical mapping systems are affected by noise, limited by resolution, and susceptible to artefacts. These will all affect the quality of the image, the segmentation, the mesh and finally the simulation predictions.

In this study, we consider the specific case of left atrial electrophysiology simulations. However, the approach could be generalised to the ventricles or other organ systems. Previous atrial electrophysiology models have been created from CT data (Fastl et al., 2018), MRI data (Roney et al., 2018) and electro-anatomical mapping data (Corrado et al., 2018a). However, the uncertainty in these images and mapping systems have not been considered when interpreting simulation predictions. In this paper, we first derive a method for estimating the left atrium anatomy in a probabilistic way; our approach quantifies the shape uncertainty. We describe the uncertainty that is generated by the composition of several sources (artefacts, inter- and intraobserver variability ...) with a single term and estimate its distribution. Then, we validate the method using images from 130 clinical cases: 70 for training and

\* Corresponding author.

E-mail address: [cesare.corrado@kcl.ac.uk](mailto:cesare.corrado@kcl.ac.uk) (C. Corrado).

60 for testing. Finally, we quantify the effect of uncertain shape on simulations of local activation time.

## 2. Methodology

In this section, we introduce a method to characterise the uncertainty about the true anatomy  $\mathbf{X}$  given an observation  $\mathbf{X}_{\text{obs}}$ . Atrial shapes are often represented using a 2D Delaunay triangulation formed from thousands of points. Previous work (Lewandowski et al., 2013; Varela et al., 2017; Biegging et al., 2018) has shown that variability in atrium and ventricular anatomies can be accurately described through 10–20 parameters using principal components (Hotelling (1933)). We adopt this approach and characterise the shape  $\mathbf{X}$  through the use of a projection into the space defined by the principal components (Hotelling, 1933), and describe uncertainty about the shape using a statistical model which we analyse in a Bayesian framework, i.e., we find the posterior probability  $p(\mathbf{X}|\mathbf{X}_{\text{obs}})$ . Unknown hyper-parameters and the reduced dimensional subspace, are estimated from a library of atrial MRI measurements.

### 2.1. Description of left atrium anatomy library

We collected atrial MRI data from 130 patients with in-plane resolution of 0.94 mm and slice thickness of 2 mm, and segmented the left atrium (LA) using a semiautomatic workflow (Razeghi et al., 2017). With the same platform, we cropped the left atrial appendage and pulmonary veins at the ostium and removed the mitral valve from the shell. The atrial shapes do not include the left atrial appendage. A rounder LA shape with a shorter, more laterally rotated appendage is predictive of AF recurrence, (Biegging et al., 2018); however, the lack of full coverage using MRI and the large variability of the appendage morphology, made it difficult to include its variability within the model. We chose to increase the number of images available to us at the expense of not including the left atrial appendage. Hence, we currently focus on the left atrial body shape only. For each cropped segmentation, we next generated a 2D triangle element shell mesh using a marching cube algorithm within the MIRTk as opposed to group. We then built an atlas mesh formed by  $N_p$  points and registered each patient's atria to the atlas by minimising the distance between the two manifolds using the diffeomorphism method implemented in Deformetrica (Durrleman et al., 2014). Deformetrica uses the large deformation diffeomorphism metric mapping (LDDMM) algorithm (Beg et al., 2005) to compute deformations. Briefly, LDDMM computes the diffeomorphic transformation between the ambient spaces embedding the objects that minimises the distance between them. LDDMM parametrises the ambient spaces and the deformation using a set of control points and applied vectors (momenta). Deformetrica adopts the varifold distance between spaces defined in Durrleman et al. (2014), (eq 14). This provides a consistent mesh topology for representing all patient anatomies. Each patient's anatomy is then described by the same number of nodes  $N_p$  by a vector  $[x_1, \dots, x_{N_p}, y_1, \dots, y_{N_p}, z_1, \dots, z_{N_p}]^T$  of the x, y and z coordinates of the deformed atlas obtained by unrolling the point coordinates. We define by  $\mathbf{X}_{\text{obs}} \in \mathbb{R}^{3N_p}$  the point coordinates of the atlas mesh after registration onto the reference mesh topology. We then divide the data in a training set of  $M = 70$  anatomies and a test set of  $M_{\text{test}} = 60$  anatomies. This gives us our libraries  $\mathbf{X}_{\text{obs}}^1, \dots, \mathbf{X}_{\text{obs}}^M$  and  $\mathbf{X}_{\text{obs}}^{M+1}, \dots, \mathbf{X}_{\text{obs}}^{M+M_{\text{test}}}$  of observed atrial anatomies.

We use  $\boldsymbol{\mu}$  to denote the average atrial anatomy (the population mean) and estimate this by the sample mean shape

$$\hat{\boldsymbol{\mu}} = \bar{\mathbf{X}}_{\text{obs}} = \frac{1}{M} \sum_{m=1}^M \mathbf{X}_{\text{obs}}^m.$$

### 2.2. Statistical model of atrial anatomy

We assume the measured anatomy  $\mathbf{X}_{\text{obs}}$  is a noisy version of the true anatomical shape

$$\mathbf{X}_{\text{obs}} = \mathbf{X} + \mathbf{e} \quad (1)$$

where  $\mathbf{e}$  is a random error, here assumed to be normally distributed with zero mean and (unknown) covariance  $\Sigma_{\mathbf{X}}$ . The aim of our analysis is to characterise the uncertainty about  $\mathbf{X}$  given the measurement  $\mathbf{X}_{\text{obs}}$ . We take a Bayesian approach and compute the posterior

$$\pi(\mathbf{X} | \mathbf{X}_{\text{obs}}) \propto \pi(\mathbf{X}_{\text{obs}} | \mathbf{X})\pi(\mathbf{X})$$

where  $\pi(\mathbf{X})$  is a prior distribution over left atrium shapes, and  $\pi(\mathbf{X}_{\text{obs}}|\mathbf{X})$  is the likelihood of observing measurement  $\mathbf{X}_{\text{obs}}$  if the true shape is  $\mathbf{X}$ . The resolution of the measurements means that the space of possible shapes is high dimensional ( $3N_p \approx 40,000$ ) making it difficult to characterise the uncertainty about the shape naively in this high dimensional space (with only  $M = 70$  measurements), and so we seek to reduce the dimension of the problem. We work in a reduced subspace of dimension  $N_{\text{modes}} \ll 3N_p$  and suppose that this subspace has a basis  $\{\mathbf{u}_1, \dots, \mathbf{u}_{N_{\text{modes}}}\}$  where  $\mathbf{u}_j \in \mathbb{R}^{3N_p}$ . We then represent  $\mathbf{X}$  as

$$\begin{aligned} \mathbf{X} &= \boldsymbol{\mu} + \sum_{i=1}^{N_{\text{modes}}} \lambda_i \mathbf{u}_i + \mathbf{e}_{\perp} \\ &= \boldsymbol{\mu} + U\boldsymbol{\lambda} + \mathbf{e}_{\perp} \end{aligned} \quad (2)$$

where  $\boldsymbol{\lambda} = (\lambda_1, \dots, \lambda_{N_{\text{modes}}})^T$  is the coordinate of  $\mathbf{X}$  in the subspace,  $U = [\mathbf{u}_1, \dots, \mathbf{u}_{N_{\text{modes}}}] \in \mathbb{R}^{3N_p \times N_{\text{modes}}}$ , and  $\mathbf{e}_{\perp}$  is an error term representing the error that arises from restricting our attention to this reduced space of anatomies.

We assume the following prior distribution on  $\boldsymbol{\lambda}$

$$\boldsymbol{\lambda} \sim N(\mathbf{0}, \Sigma_{\boldsymbol{\lambda}}). \quad (3)$$

From the definition (2), it follows that also  $\mathbf{e}_{\perp}$  can be represented as a linear combination of modes:  $\mathbf{e}_{\perp} = U_{\perp} \boldsymbol{\lambda}_{\perp}$ . Here  $U_{\perp} = [\mathbf{u}_{N_{\text{modes}}+1}, \dots, \mathbf{u}_{N_{\text{modes}}+3N_p}]$  is a basis of the subspace that is orthogonal to the subspace generated by  $U$ , while  $\boldsymbol{\lambda}_{\perp}$  are the coordinates of  $\mathbf{X}$  in this subspace. As in Eq. (3), we make the assumption  $\boldsymbol{\lambda}_{\perp} \sim N(\mathbf{0}, \Sigma_{\boldsymbol{\lambda}_{\perp}})$ . Combining these assumptions, we obtain:

$$\mathbf{e}_{\perp} \sim N(\mathbf{0}, \Sigma_{\mathbf{e}_{\perp}}), \quad \Sigma_{\mathbf{e}_{\perp}} = U_{\perp} \Sigma_{\boldsymbol{\lambda}_{\perp}} U_{\perp}^T.$$

It is conceptually possible to determine  $\Sigma_{\boldsymbol{\lambda}_{\perp}}$  following the procedure we propose in Section 2.5. However, this would require a training set with  $M \geq 3N_p$  samples (for the current shape model this would be 40,707 segmentations).

Combining Eqs. (1) and (2) gives

$$\mathbf{X}_{\text{obs}} = \boldsymbol{\mu} + U\boldsymbol{\lambda} + \mathbf{e}_{\text{TOT}} \quad (4)$$

where  $\mathbf{e}_{\text{TOT}} = \mathbf{e}_{\perp} + \mathbf{e}$ , which has a zero-mean Gaussian distribution

$$\mathbf{e}_{\text{TOT}} \sim N(\mathbf{0}, \Sigma_{\mathbf{e}_{\text{TOT}}}) \quad (5)$$

where  $\Sigma_{\mathbf{e}_{\text{TOT}}}$  is a covariance matrix we define below.

Eqs. (3)–(5) define our statistical model. We use the training library of observed atrial anatomies to estimate all of the unknown parameters,  $\Sigma_{\boldsymbol{\lambda}}$ ,  $\Sigma_{\mathbf{e}_{\text{TOT}}}$ , and  $\boldsymbol{\mu}$ , as well as the reduced order basis  $U$  (see Section 2.3). Given values for these parameters, we can then solve the Bayesian updating problem to compute the posterior distribution for the unknown coordinates in the reduced space  $\pi(\boldsymbol{\lambda}|\mathbf{X}_{\text{obs}}) = \pi(\mathbf{X}_{\text{obs}} | \boldsymbol{\lambda})\pi(\boldsymbol{\lambda})/\pi(\mathbf{X}_{\text{obs}})$  and then compute the uncertainty about the unknown shape  $\mathbf{X}$  via

$$\pi(\mathbf{X} | \mathbf{X}_{\text{obs}}) = \int \pi(\mathbf{X} | \boldsymbol{\lambda})\pi(\boldsymbol{\lambda} | \mathbf{X}_{\text{obs}})d\boldsymbol{\lambda}.$$

This is described in Section 2.5.

### 2.3. Estimation of the reduced space

We limit our interest to the affine space formed by the columns of  $U$ , i.e., we consider shapes of the form

$$\boldsymbol{\mu} + \sum_{i=1}^{N_{\text{modes}}} \lambda_i \mathbf{u}_i$$

for all possible values of  $\boldsymbol{\lambda}$ . We use the training library of the measured anatomies to select the basis vectors  $U$  using principal component analysis (PCA). If

$$\widehat{\Sigma} = \frac{1}{M-1} \sum_{k=1}^M (\mathbf{X}_{\text{obs}}^k - \widehat{\boldsymbol{\mu}})(\mathbf{X}_{\text{obs}}^k - \widehat{\boldsymbol{\mu}})^\top$$

is the sample covariance matrix of the  $M$  library shapes, then the principal components are the eigenvectors of  $\widehat{\Sigma}$ . For reasons of numerical stability and efficiency, we work with the singular value decomposition of

$$\begin{aligned} A_{\text{obs}} &:= [\mathbf{X}_{\text{obs}}^1 - \widehat{\boldsymbol{\mu}} \dots \mathbf{X}_{\text{obs}}^M - \widehat{\boldsymbol{\mu}}] \\ &= U\Theta V^\top. \end{aligned} \quad (6)$$

Here  $U = [\mathbf{u}_1 \dots \mathbf{u}_M]$  is the  $3N_p \times M$  matrix containing the principal components (PCs), which we truncate to only include the first  $N_{\text{modes}}$  modes of the decomposition. The PCs are ordered in order of decreasing singular values, so that  $\mathbf{u}_1$  is the direction in the data in which the data are most variable. This truncation is the optimal compression of  $A_{\text{obs}}$  in terms of minimizing the Frobenius norm (essentially the  $L_2$ -norm for matrices) of the approximation error. The number of modes,  $N_{\text{modes}}$ , for describing the atrial anatomy was set to capture  $\approx 95\%$  of the shape variance.

### 2.4. Variance matrices

We need to specify the covariance matrix  $\Sigma_{\mathbf{e}_{\text{TOT}}}$  for the error term in Eq. (5). This error term consists of the observation error and the truncation error that occurs due to restricting our attention to the subspace  $\text{span}(U)$ . Instead of using the structure in  $\mathbf{e}_\perp$ , which is computationally burdensome to deal with, we model the covariance structure of  $\mathbf{e}_{\text{TOT}}$  using a standard covariance model. We make the assumption that the correlation between errors at different locations is a monotone decreasing function of the (geodesic) distance between the locations. In particular, we use a Matérn covariance (Minasy and McBratney (2005)) function to characterise  $\Sigma_{\mathbf{e}_{\text{TOT}}}$ , as this gives an error that is spatially continuous, but nowhere differentiable (i.e., not smooth). This covariance function has two parameters:

$$\Sigma_{\mathbf{e}_{\text{TOT}}}^{i_{x_k}, j_{x_l}} = \nu^2 \exp\left(-\frac{d_{ij}}{l}\right) \delta_{x_k, x_l} \quad (7)$$

Here,  $\nu^2$  represents the variance of the error,  $l$  the characteristic length of the spatial correlation, and  $d_{ij}$  the geodesic distance between points  $i$  and  $j$  evaluated on the mean shape  $\boldsymbol{\mu}$ .  $\delta_{x_k, x_l}$  is the Kronecker delta between the space components  $x_k$  and  $x_l$ , and index  $i_{x_k}$  represents the entry in  $\Sigma_{\mathbf{e}_{\text{TOT}}}$  corresponding to node  $i$  and component  $x_k$ .

To simplify the calculation we definex

$$\mathbf{X}_{\text{obs}}^{\text{reduced}} = U^\top (\mathbf{X}_{\text{obs}} - \boldsymbol{\mu})$$

to be the projection of  $\mathbf{X}_{\text{obs}}$  into the reduced space. Then

$$\mathbf{X}_{\text{obs}}^{\text{reduced}} | \boldsymbol{\lambda} \sim N(\boldsymbol{\lambda}, U^\top \Sigma_{\mathbf{e}_{\text{TOT}}} U)$$

by Eq. (5). If we assume  $\boldsymbol{\lambda} \sim N(\mathbf{0}, \Sigma_\lambda)$  then marginalising out the dependence on  $\boldsymbol{\lambda}$  gives

$$\mathbf{X}_{\text{obs}}^{\text{reduced}} \sim N(\mathbf{0}, U^\top \Sigma_{\mathbf{e}_{\text{TOT}}} U + \Sigma_\lambda).$$

We then estimate  $\nu^2$  and  $l$  by their maximum likelihood estimates

$$\nu^2, l = \arg \max \log L(\nu^2, l; \mathbf{X}_{\text{obs}}^{\text{reduced}})$$

which we compute using STAN (Carpenter et al., 2017) after first transforming to

$$p_l = \log(l) \quad p_{\nu^2} = \log(\nu^2)$$

to ensure positivity.

### 2.5. Bayesian inference of the posterior distribution for $\boldsymbol{\lambda}$ and $\mathbf{X}$

The uncertainty in the shape is characterised by the uncertainty on the  $\boldsymbol{\lambda}$  values. We infer the  $\boldsymbol{\lambda}$  values within a Bayesian framework, updating a prior distribution with observations to obtain the posterior distribution for  $\boldsymbol{\lambda}$ . A priori, we assume the components of  $\boldsymbol{\lambda}$  are mutually independent and normally distributed (Eq. 3). To specify  $\Sigma_\lambda$  we use  $\Theta$ , the matrix of singular values obtained in Eq. (6). These values are proportional to the standard deviation associated with each principal component. We set

$$\sigma_i^2 = \frac{\Theta_i^2}{M-1}$$

and let  $\Sigma = \text{diag}(\sigma_1, \dots, \sigma_{N_{\text{modes}}})$ . We set  $\Sigma_\lambda = \Sigma^\top \Sigma$  and use  $\hat{\boldsymbol{\lambda}} = \Sigma^{-1} \boldsymbol{\lambda}$  to denote the standardised coordinates so that if  $\boldsymbol{\lambda} \sim N(\mathbf{0}, \Sigma_\lambda)$  then  $\hat{\boldsymbol{\lambda}} \sim N(\mathbf{0}, I)$ . We test the reasonableness of this prior distribution by estimating the coordinates using

$$\hat{\boldsymbol{\lambda}}^i = \Sigma^{-1} U^\top (\mathbf{X}_{\text{obs}}^i - \boldsymbol{\mu}), \quad i = 1 \dots M$$

for the atrial library, and then testing whether the  $\hat{\boldsymbol{\lambda}}_j^i$  are indistinguishable from a sample of independent  $N(0, 1)$  random variables using a Kolmogorov Smirnov test.

We experimented with adding an additional degree of freedom into the model to inflate or deflate the prior variance by using the prior distribution  $\hat{\boldsymbol{\lambda}} \sim N(\mathbf{0}, \alpha^2 I)$ , and determine  $\alpha$  using the training set. In this case, we obtain  $\Sigma_\lambda = \alpha^2 \Theta^\top \Theta$ . (See Appendix A for details.)

To compute the posterior distribution, we note that the prior distribution and the likelihood are both Gaussian, hence the problem is conjugate and we obtain a normal distribution for the posterior distribution. To see this, note that

$$\begin{aligned} \pi(\boldsymbol{\lambda}) &\propto \exp\left(-\frac{1}{2} \boldsymbol{\lambda}^\top \Sigma_\lambda^{-1} \boldsymbol{\lambda}\right) \\ \pi(\mathbf{X}_{\text{obs}} | \boldsymbol{\lambda}) &\propto \exp\left(-\frac{1}{2} (\mathbf{X}_{\text{obs}} - \boldsymbol{\mu} - U\boldsymbol{\lambda})^\top \Sigma_{\mathbf{e}_{\text{TOT}}}^{-1} (\mathbf{X}_{\text{obs}} - \boldsymbol{\mu} - U\boldsymbol{\lambda})\right). \end{aligned}$$

Hence

$$\begin{aligned} \pi(\boldsymbol{\lambda} | \mathbf{X}_{\text{obs}}) &\propto \exp\left(-\frac{1}{2} \boldsymbol{\lambda}^\top \Sigma_\lambda^{-1} \boldsymbol{\lambda}\right) \exp\left(-\frac{1}{2} (\mathbf{X}_{\text{obs}} - \boldsymbol{\mu} - U\boldsymbol{\lambda})^\top \Sigma_{\mathbf{e}_{\text{TOT}}}^{-1} (\mathbf{X}_{\text{obs}} - \boldsymbol{\mu} - U\boldsymbol{\lambda})\right) \\ &\quad \times (\mathbf{X}_{\text{obs}} - \boldsymbol{\mu} - U\boldsymbol{\lambda}) \\ &\propto \exp\left(-\frac{1}{2} (\boldsymbol{\lambda}^\top \Sigma_\lambda^{-1} \boldsymbol{\lambda} + (\mathbf{X}_{\text{obs}} - \boldsymbol{\mu} - U\boldsymbol{\lambda})^\top \Sigma_{\mathbf{e}_{\text{TOT}}}^{-1} (\mathbf{X}_{\text{obs}} - \boldsymbol{\mu} - U\boldsymbol{\lambda}))\right) \\ &\propto \exp\left(-\frac{1}{2} (\boldsymbol{\lambda}^\top (\Sigma_\lambda^{-1} + U^\top \Sigma_{\mathbf{e}_{\text{TOT}}}^{-1} U) \boldsymbol{\lambda} - 2\boldsymbol{\lambda}^\top U^\top \Sigma_{\mathbf{e}_{\text{TOT}}}^{-1} (\mathbf{X}_{\text{obs}} - \boldsymbol{\mu}) + \text{const})\right) \\ &\propto \exp\left(-\frac{1}{2} (\boldsymbol{\lambda}^\top \Sigma_{\boldsymbol{\lambda}, \text{post}}^{-1} \boldsymbol{\lambda} - 2\boldsymbol{\lambda}^\top \Sigma_{\boldsymbol{\lambda}, \text{post}}^{-1} \boldsymbol{\mu}_{\text{post}} + \text{const})\right) \end{aligned}$$

where  $\text{const}$  represents the integration constant. We thus obtain the posterior distribution for  $\boldsymbol{\lambda}$ :

$$\boldsymbol{\lambda} | \mathbf{X}_{\text{obs}} \sim N(\boldsymbol{\mu}_{\text{post}}, \Sigma_{\boldsymbol{\lambda}, \text{post}}) \quad (8)$$

where

$$\Sigma_{\lambda, \text{post}} = (\Sigma_{\lambda}^{-1} + U^T \Sigma_{e_{\text{TOT}}}^{-1} U)^{-1}$$

$$\mu_{\text{post}} = \Sigma_{\lambda, \text{post}} U^T \Sigma_{e_{\text{TOT}}}^{-1} (\mathbf{X}_{\text{obs}} - \mu).$$

Finally, we obtain:

$$\mathbf{X} | \mathbf{X}_{\text{obs}} \sim N(\hat{\mu} + U \mu_{\text{post}}, U \Sigma_{\lambda, \text{post}} U^T)$$

by marginalising out the dependence on  $\lambda$ . We provide details on the inversion of  $\Sigma_{e_{\text{TOT}}}$  in [Appendix B](#).

### 2.6. Quantification of the uncertainty on simulations

Anatomy uncertainty affects numerical simulations of cardiac electrophysiology as the anatomical mesh may change size and shape. Denoting by  $y = f(\mathbf{X})$  the generic solution of a numerical simulation defined on the uncertain domain  $\mathbf{X}$ , we can evaluate the expected value  $\mathbb{E}[y|\mathbf{X}_{\text{obs}}]$  and the variance  $\text{Var}[y|\mathbf{X}_{\text{obs}}]$  using Monte Carlo. Once a new anatomy  $\mathbf{X}_{\text{obs}}$  is measured with MRI, we first evaluate the posterior distribution (8); next, we draw  $N_{\text{samples}}$  independent and identically distributed (i.i.d.) random samples from  $\pi(\lambda|\mathbf{X}_{\text{obs}})$  and we obtain the anatomy samples  $(\mathbf{X}^1, \dots, \mathbf{X}^{N_{\text{samples}}})$  as  $\mathbf{X}^k = \mu + U\lambda^k$ . We then check the consistency of each sample  $\mathbf{X}^k$  using the following methodology: for each triangle  $\mathcal{T}_j^k$  forming the 2D manifold, we evaluate 1) the ratio  $A_j^k/A_j^{\text{REF}}$  between the area  $A_j^k$  of the  $j$ th triangle in the  $k$ th sample and the area  $A_j^{\text{REF}}$  of the  $j$ th triangle on the mean shape. Whenever  $A_j^k/A_j^{\text{REF}}$  approaches 0, the  $j$ th triangle degenerates and the sample is inconsistent and thus discarded. We then evaluate 2) the dot product  $\vec{N}_j^k \cdot \vec{N}_j^{\text{REF}}$  between the normal  $\vec{N}_j^k$  of the  $j$ th triangle in the  $k$ th sample and the normal  $\vec{N}_j^{\text{REF}}$  of the  $j$ th triangle on the mean shape. Whenever  $\vec{N}_j^k \cdot \vec{N}_j^{\text{REF}}$  becomes negative, at least one point in the  $j$ th triangle is displaced into another element: the sample is inconsistent and thus discarded. This ensures that each sample is a consistent mesh.

On each sample anatomy we evaluate the sample solution  $y^i = f(\mathbf{X}^i)$ , and finally we use the Monte Carlo approximations

$$\mathbb{E}[y|\mathbf{X}_{\text{obs}}] \approx \frac{1}{N_{\text{samples}}} \sum_{i=1}^{N_{\text{samples}}} y^i,$$

$$\text{Var}[y|\mathbf{X}_{\text{obs}}] \approx \frac{1}{N_{\text{samples}} - 1} \sum_{i=1}^{N_{\text{samples}}} (y^i - \mathbb{E}[y|\mathbf{X}_{\text{obs}}])^2$$

to compute the estimated posterior mean and variances.

## 3. Results

### 3.1. Generating the left atrium mean shape

[Table 1](#) summarises the characteristics of the patients included in this study. Following the procedure described in [Section 2.1](#), we

**Table 1**

Patient statistics. (BMI=Body mass index. EDV=end diastolic volume. ESV=End systolic volume. PAF=Paroxysmal atrial fibrillation. PsAF=Persistent atrial fibrillation.).

Quantity	training set (70 patients)	test set (60 patients)
Female	45%	31%
PAF	43.33%	50%
PsAF	23.33%	50%
Control	33.33%	0%
age	61( $\pm$ 11)	64( $\pm$ 10)
weight(kg)	82( $\pm$ 15)	87( $\pm$ 15)
height(cm)	172( $\pm$ 11)	175( $\pm$ 9)
BMI	28( $\pm$ 7)	29( $\pm$ 5)
LA EDV(ml)	63( $\pm$ 27)	81( $\pm$ 33)
LA ESV(ml)	104( $\pm$ 29)	119( $\pm$ 27)

first generated 130 meshes ( $19,359 \pm 8,047$  vertices) from clinical MRI images; next, we registered all the 130 meshes to an atlas formed by  $N_p = 13,569$  vertices.

[Fig. 1](#) shows the sample mean shape generated from the 70 atrial anatomies used as a training set. On the same figure, we marked the left atrial appendage (LAA), the mitral valve (MV) and each of the four pulmonary veins (PV).

### 3.2. Anatomical model reduction

We applied PCA to reduce the number of parameters describing the shape. [Fig. 2 -A](#) shows the ratio between  $\sigma_1^2$  captured by each component and the largest value of  $\sigma^2$  that corresponds to the first component. Using 15 modes we captured  $\approx 95\%$  of the shape variance.

To provide a representation of each mode, we calculated the displacement of the  $i$ -th mode at each vertex as:  $\mathbf{d} = \sigma_i \mathbf{u}_i$ , obtaining the unrolled vector:  $([d_1^x, \dots, d_{N_p}^x, d_1^y, \dots, d_{N_p}^y, d_1^z, \dots, d_{N_p}^z]^T) \in \mathbb{R}^{3N_p}$ . [Fig. 3](#) shows the map of the displacement magnitude for each of the 15 modes.

We then checked whether the chosen number of modes was independent of the training set size, as described in [Section 2.3](#). [Fig. 2 -B](#) shows the values of  $\sigma_i^2/\sigma_1^2$  and their confidence intervals when the training set is formed by 31, 41, 51 or all patient cases. For all the sample sizes tested, we capture  $\approx 95\%$  of the shape variance using 15 modes.

### 3.3. Validation of reduced anatomy representation

We tested the suitability of the proposed reduced representation model using  $k$ -fold cross-validation ([Stone, 1974](#)). First, we divide the training set into  $k = 10$  folds, each one formed by  $M/k = 7$  samples. Next, we train the model using the samples arising from  $(k - 1)$  folds and we evaluate the truncation error on each sample in the fold that has not been used for training. We repeat the procedure  $k$  times selecting each fold as a test set. Once all the  $k$  folds have been tested, we then shuffle the samples in the data set

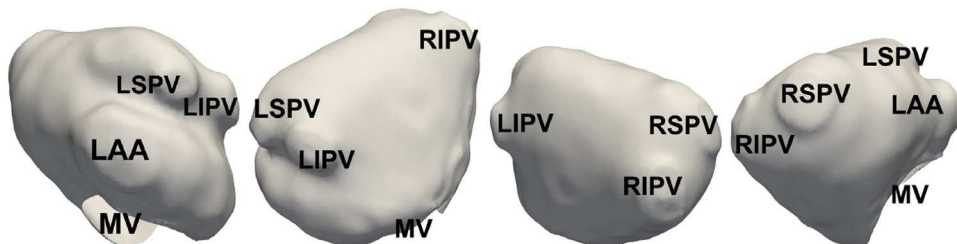


**Fig. 1.** Sample mean evaluated from 70 meshes used for training data. On the same shape, we marked the left atrial appendage (LAA), the left superior pulmonary vein (LSPV), the left inferior pulmonary vein (LIPV), the right superior pulmonary vein (RSPV), the right inferior pulmonary vein (RIPV) and the mitral vale (MV).

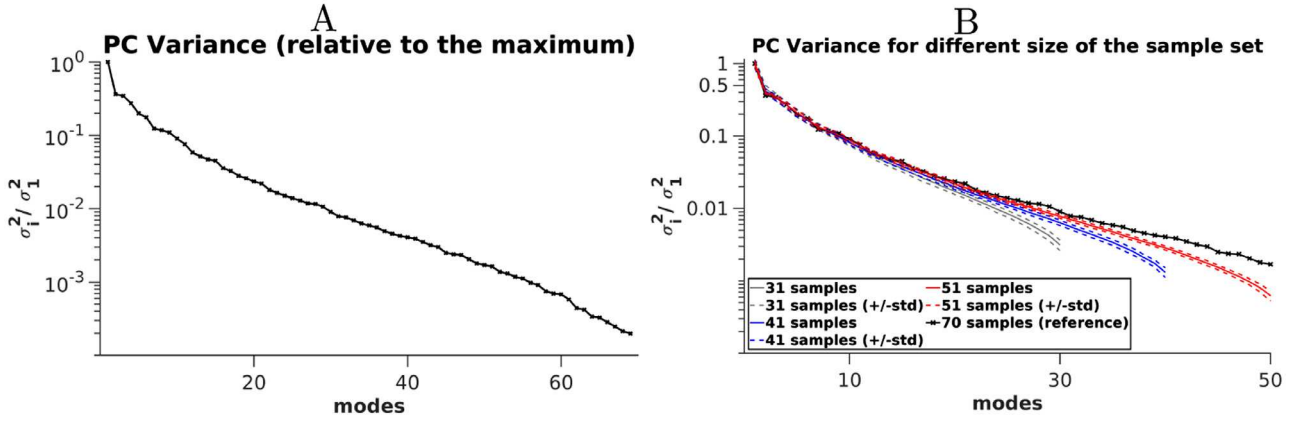


Fig. 2. A: logarithmic plot of  $\sigma_i^2/\sigma_1^2$  when considering all 70 data sets. B: logarithmic plot of  $\sigma_i^2/\sigma_1^2$ , evaluated by varying the number of samples; dashed lines represent the confidence interval.

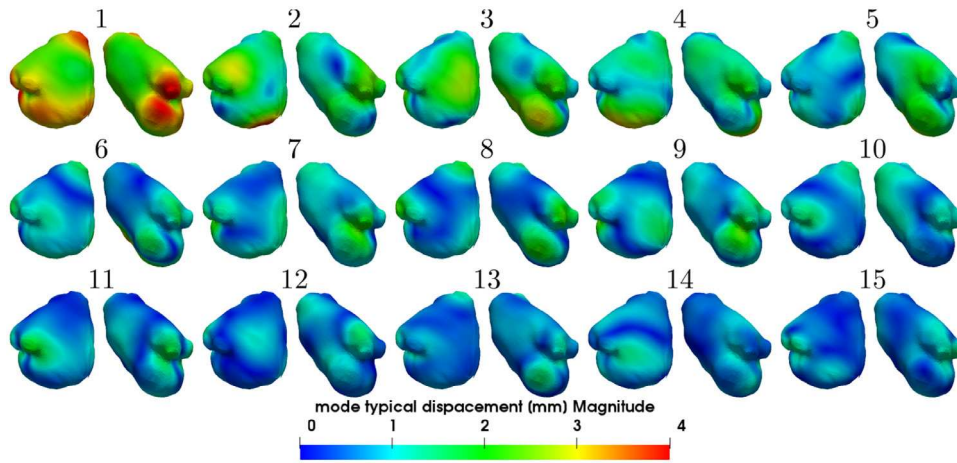


Fig. 3. Map of the magnitude of the displacement  $\mathbf{d} = \sigma_i \mathbf{u}_i$ , for each of the 15 modes.

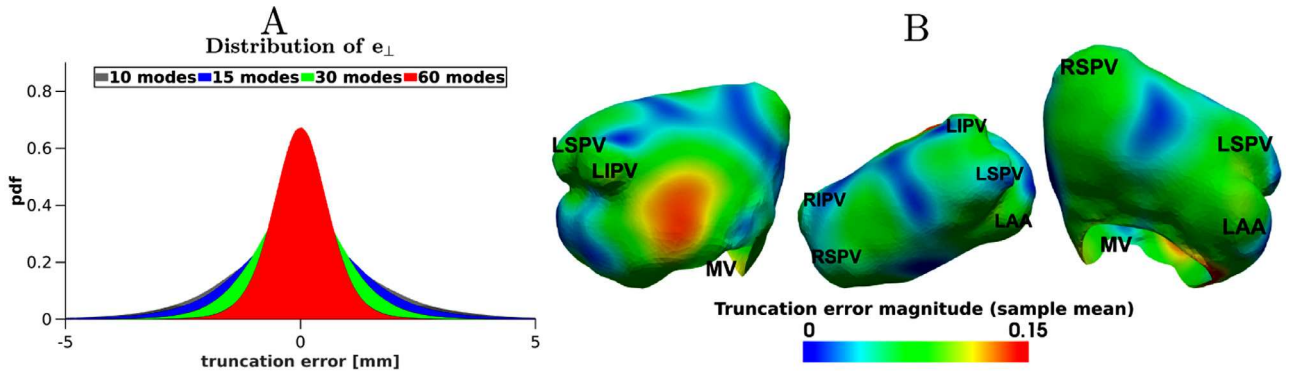


Fig. 4. A: plot of the distribution of the truncation error. B: Magnitude field of the mean of the truncation error evaluated when describing the anatomy with 15 modes. We marked the left atrial appendage (LAA), the left superior pulmonary vein (LSPV), the left inferior pulmonary vein (LIPV), the right superior pulmonary vein (RSPV), the right inferior pulmonary vein (RIPV) and the mitral vale (MV).

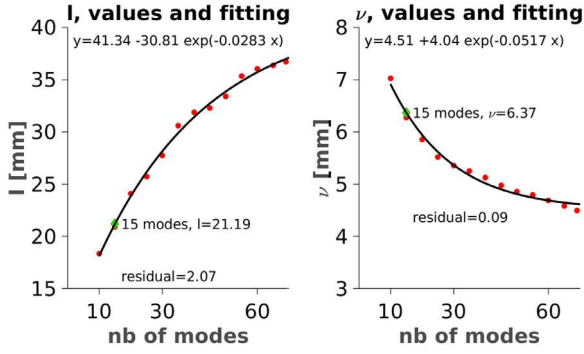
with a random permutation and we repeat the procedure. We test a total of  $N_{perm} = 20$  random permutations; at the end, we obtain  $N_{perm} \times (M/k) \times k = N_{perm} \times M = 1400$  truncation error vectors. Finally, we collect all the entries of the truncation error vectors in a unique set, hence formed by  $N_{perm} \times M \times 3N_p$  samples and we evaluate the sample mean and the sample standard deviation. Fig. 4 - A shows the distribution of the truncation error for 10, 15, 30 and 60 modes. This test demonstrates that the truncation error converges to a distribution that has a zero mean and a standard deviation that decreases when increasing the number of modes.

Table 2

Mean and standard deviation of the truncation error using 10, 15, 30 and 60 modes respectively.

nb of modes	10	15	30	60
mean	0.0	0.0	0.0	0.0
standard deviation	1.64	1.4	1.01	0.66

Table 2 reports the mean and standard deviation of the truncation error using 10, 15, 30 and 60 modes.



**Fig. 5.** Parameter values evaluated with the maximum joint posterior estimation algorithm (red dots) fitted expression (black line). Left panel represents the characteristic distance  $l$ ; right panel the typical standard deviation,  $\nu$ . The green diamonds represent the fitting with  $N_{\text{modes}} = 15$ . (For interpretation of the references to colour in this figure legend, the reader is referred to the web version of this article.)

Next, we evaluated the vector field of the mean of the truncation error for a shape description with 15 modes and we plotted the vector magnitude field onto the reference atlas (Fig. 4 - B).

### 3.4. Fitting the combined truncation error and measurement uncertainty model

We evaluated the value of the parameters ( $l$ ,  $\nu$ ) that characterise the covariance matrix (7) using the procedure described in Section 2.4. Next, we fitted exponential functions to characterise the parameter values as a function of the number of modes. Fig. 5 shows the parameter values evaluated using the maximum joint posterior estimation algorithm implemented in STAN (Carpenter et al., 2017) (red dots) and the fitted expression (black line). Asymptotically, the two parameters approach  $l \rightarrow 41.34$  mm and  $\nu \rightarrow 4.51$  mm.

When we approximate the shape using 15 modes, we found  $l = 20.91$  mm and  $\nu = 6.28$  mm. Fig. 5 shows the value of the fitting when  $N_{\text{modes}} = 15$  (green diamonds).

### 3.5. Reduced dimensionality shape prior

To test if the shape population can be represented using the distribution  $\hat{\lambda} \sim N(\mathbf{0}, I)$ , we first calculated  $\hat{\lambda}$  for each of the 70 training set cases and evaluate the sample mean and the sample standard deviation giving  $\mu_{\hat{\lambda}} \approx 1e^{-17}$  and  $\sigma_{\hat{\lambda}} \approx 0.99$ . Testing for normality we found no evidence to reject the null hypothesis

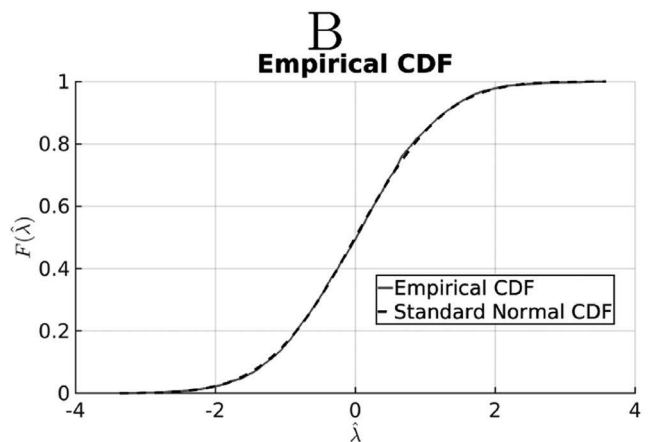
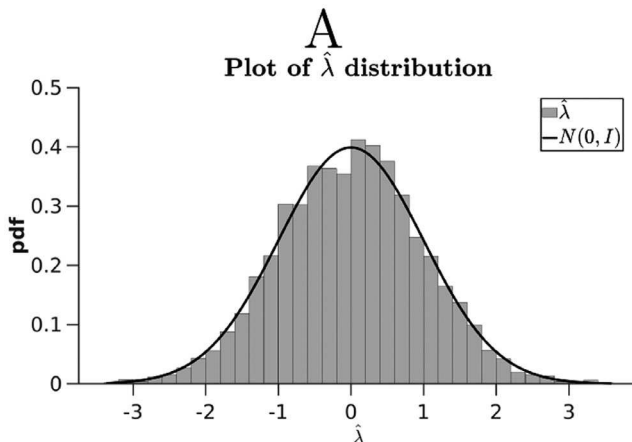


**Fig. 6.** A: Histogram plot of the distribution of  $\hat{\lambda}$ ; the black line represents the normal distribution  $N(0, 1)$ . B: QQ plot of the empirical cumulative density function (cdf) and the standard normal cdf.

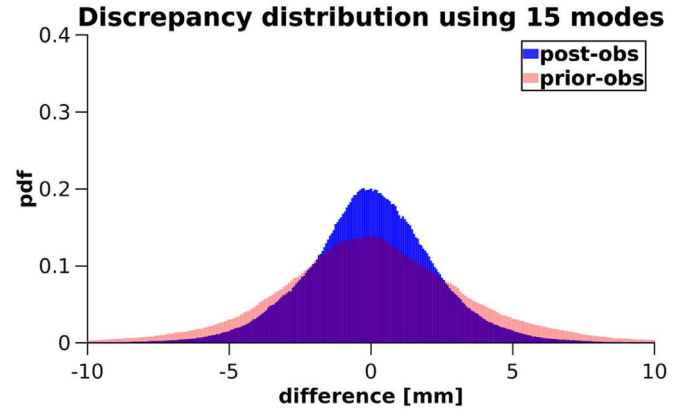


**Fig. 7.** Distribution of the discrepancy between the measurements and the posterior anatomies (blue bars) and of the discrepancy between the measurements and the mean shape (red bars). (For interpretation of the references to colour in this figure legend, the reader is referred to the web version of this article.)

( $p=0.30$ ). The histogram plot (Fig. 6 -A) and the QQ plot (Fig. 6 -B) for  $\hat{\lambda}$  showed excellent agreement with a standard normal distribution. This confirms that we can represent the population distribution using a normal distribution.

### 3.6. Estimating shape posterior

We tested the performances of the algorithm presented here on the test set of  $M_{\text{test}} = 60$  clinical MRI datasets. None of the samples of the test set were used to train the model. We evaluated the discrepancies  $\mathbf{X}_{\text{post}}^k - \mathbf{X}_{\text{obs}}^k$ ,  $k = 1 \dots M_{\text{test}}$  between the measurements and the posterior anatomies and we compared with the discrepancies  $\boldsymbol{\mu} - \mathbf{X}_{\text{obs}}^k$  between the measurements and the prior (mean) anatomy. Next, we compared the projection of the observations on the modes  $\boldsymbol{\lambda}_{\text{obs}} = \mathbf{U}^T (\mathbf{X}_{\text{obs}} - \boldsymbol{\mu})$  with the posterior expected value  $\boldsymbol{\mu}_{\text{post}}$  and with the 95% confidence interval (CI), evaluated on the marginal distribution, as  $\lambda_i^{\text{post}, \pm 95\text{CI}} = (\boldsymbol{\mu}_{\text{post}})_i \pm 1.96 \sqrt{(\boldsymbol{\Sigma}_{\boldsymbol{\lambda}, \text{post}})_{ii}}$ .

Fig. 7 shows the overall distribution of the discrepancies, for all the  $M_{\text{test}}$  cases and all the  $3N_p$  components. We found discrepancies distributed with a null mean and a standard deviation of 2.34 mm (blue bars). The discrepancy with the mean shape has a distribution with a null mean and a standard deviation of 3.51 mm (red bars). Fig. 8 shows the projection  $\boldsymbol{\lambda}_{\text{obs}}$  of the observations on the reduced space (black dots). On all the cases,

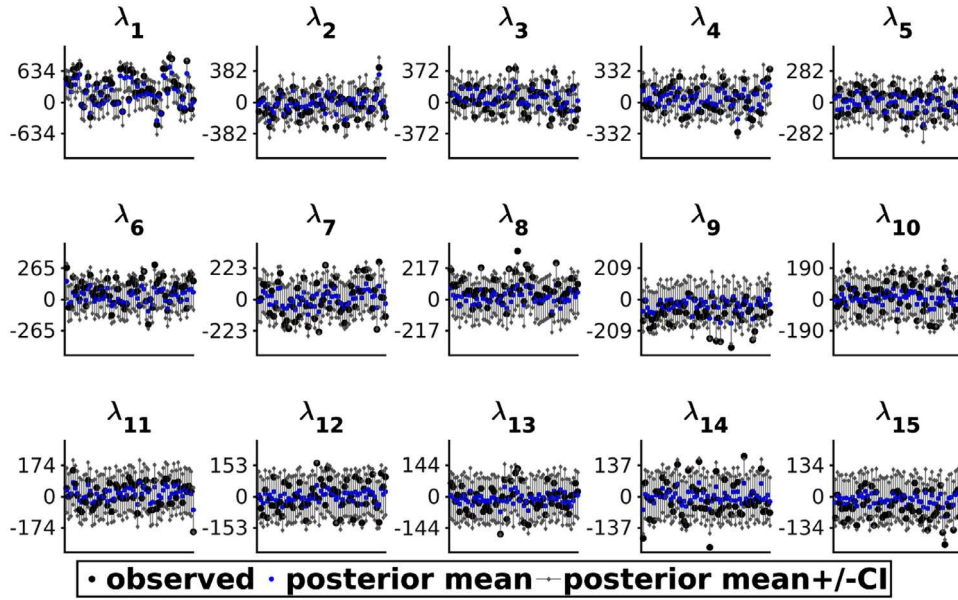


**Fig. 8.** Projection  $\lambda_{\text{obs}}$  of the observations on the reduced space (black dots) and posterior mean  $\mu_{\text{post}}$  (blue dots) for all the  $M_{\text{test}}$  test cases. The same figure depicts the 95% confidence interval  $\lambda_i^{\text{post},95\text{CI}}$  (blue bar). (For interpretation of the references to colour in this figure legend, the reader is referred to the web version of this article.)

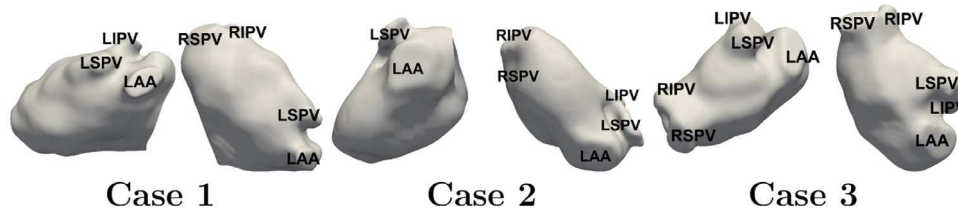


**Fig. 9.** Anatomies used to test the method in presence of artefacts.

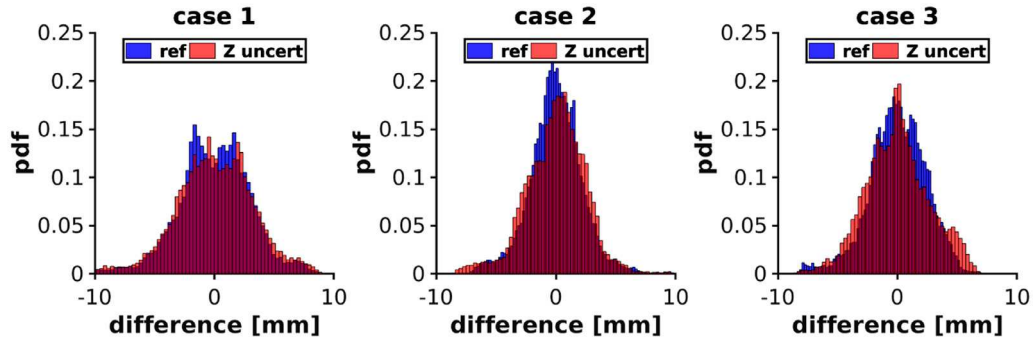


**Fig. 10.** Discrepancy distributions for each of the 3 cases when the mesh is obtained segmenting every second slice (blue bars) and every 8-th slice (red bars). (For interpretation of the references to colour in this figure legend, the reader is referred to the web version of this article.)

$\lambda_{\text{obs}} \in [\lambda_i^{\text{post},-95\text{CI}}, \lambda_i^{\text{post},+95\text{CI}}]$  for the first 5 modes, while only 4 cases showed larger discrepancies on higher modes.

We then tested the performances of the method in the presence of artefacts with the 3 new anatomies of Fig. 9 obtained from MRI.

On each of the 3 new cases, we first manually segmented every second slice and we generated the reference 2D shell meshes. We then introduced uncertainty generating the 2D shell meshes on the same images segmenting every 8-th slice, representing a 4 fold decrease in image resolution. In the meshes generated from segmenting every second slice the discrepancies between posteriors and observations presented a null mean and a standard deviation of 2.55 mm (respectively 2.98 mm for case 1, 2.22 mm for case 2 and 2.38 mm for case 3). When we use meshes obtained

from an image segmented every 8-th slice, the discrepancies between posteriors and observations overall presented a null mean and a standard deviation of 2.83 mm (respectively 3.28 mm for case 1, 2.47 mm for case 2 and 2.65 mm for case 3). Fig. 10 plots the distribution of the discrepancies for a mesh obtained segmenting every second slice (blue bars) and every 8-th slice (red bars).

### 3.7. Calculating uncertainty due to shape in electrophysiology simulations

We evaluated the impact of the shape uncertainty on electrophysiology simulations. We evaluated the expected value and the variance of the local activation times (LAT) on the 3 anatomies in-

**Table 3**

Distribution (mean and standard deviation) of sample  $A_j^k/A_j^{\text{REF}}$  and  $\bar{N}_j^k \cdot N_j^{\text{REF}}$  for each case.

Case	$(A_j^k/A_j^{\text{REF}})_{\text{mean}}$	$(A_j^k/A_j^{\text{REF}})_{\text{std}}$	$(\bar{N}_j^k \cdot N_j^{\text{REF}})_{\text{mean}}$	$(\bar{N}_j^k \cdot N_j^{\text{REF}})_{\text{std}}$
Case 1	1.34	0.26	0.98	0.02
Case 2	1.1	0.27	0.97	0.04
Case 3	1.24	0.24	0.99	0.01

troduced at the end of Section 3.6, and shown in Fig. 9, that were obtained by segmenting every second slice from the MRI dataset. For each case, we draw a total of 12,000 independent identically distributed (iid) samples from the distribution (8) and then we obtain the sample shape from (2). We then tested the sample consistency with the procedure described in Section 2.6, summarises the distribution of  $A_j^k/A_j^{\text{REF}}$  and  $\bar{N}_j^k \cdot N_j^{\text{REF}}$  for each case Table 3. All of the samples produced a valid mesh.

The  $l_2$  norm of the difference between the expected value evaluated with 12,000 samples and the expected value we obtained using 10,000 samples was  $1.58\text{ms} \pm 0.53\text{ms}$  or  $\sim 1\%$  of the total activation time. Hence, 12,000 samples are adequate to evaluate the uncertainty on LATs evaluation when the atrial shape is affected by uncertainty.

Next, we simulated the LATs using the combined eikonal solver (Corrado and Zemzemi, 2018) and modified Mitchell-Schaeffer model (Corrado and Niederer, 2016). This solver allows the evaluation of the conduction velocity directly from the model parameters. In this paper, we use the technique presented in Corrado and Zemzemi (2018) to compute LATs for a single heartbeat. The simulation was initialised by defining an activated region. We chose  $\tau_{\text{in}} = 0.1$ ,  $\tau_{\text{out}} = 2.5$  and  $v_{\text{gate}} = 0.1$  as model parameters and an isotropic diffusivity of  $\sigma_m = 1.0\text{cm}^2/\text{s}$  for the atrial tissue. No anatomically tailored fibres were generated. These parameters produce a conduction velocity comparable with human atrial myocytes, (Corrado et al., 2016; 2017). On the termination of the pulmonary veins, we chose a diffusivity of  $\sigma_m = 10^{-7}\text{cm}^2/\text{s}$  to avoid propagation in these regions. To take into account of the effect of low mesh resolution on the propagation through a graph, we set the corrective coefficient to  $\delta = 0.87$ . This value provided the minimum RMS on LATs between the solution of the eikonal model and the solution of a finite element discretization of the monodomain equations with a discretization size  $h \simeq 300\mu\text{m}$ . We assigned an initial activated region by setting the value of LAT to 0ms at a mesh point that was manually chosen on the mean shape and located in the proximity of the coronary sinus. This reflects the activation location routinely used in clinical pacing studies. Since the mesh topology is kept constant across all the samples, we automatically adopted the same mesh point as the onset for each of the eikonal model solves. We finally evaluate the expected value and the standard deviation of LATs with the formula introduced in Section 2.6.

For each of the 3 cases, Fig. 11 shows the expected value of LATs, while Fig. 12 shows the distribution of the standard deviation.

#### 4. Discussion

In this work we have developed a theoretical framework for encoding shape and shape uncertainty, we have applied this method to estimate left atrium (LA) shape and uncertainty from cardiac MRI images and used a statistical description of the LA shape to quantify how shape uncertainty affects cardiac activation simulations in the left atrium.

*Model description.* We parametrised the anatomy using the principal component analysis; this description allows characterising anatomy with a small number of parameters. The same description has been used in ventricles, (Lewandowski et al., 2013) with an atlas of 1152 points and 6 principal components and in atria, (Varela et al., 2017), registering a sphere characterised by 1608 degree of freedom on the atrium and then adopting 8 principal components. The complexity of the atrial shape and the requirement of performing simulations of the electrophysiology, however, require a larger number of points; moreover, the larger inter-individual variability required a larger number of modes. Hence, in this paper, we adopted an atlas with 13,569 nodes and 15 modes. When the cumulative explained variance is considered, 15 modes allow to capture  $\sim 90\%$ , whereas in Lewandowski et al. (2013) authors captured  $\sim 84\%$  using 6 principal components.

*Probabilistic approach* Previous studies described the left atrial shape either using a set of surface correspondence points (Biegging et al., 2018), or through cubic Hermite basis functions, (Lewandowski et al., 2013; Varela et al., 2017) and then reduced the space of the parameter of interest evaluating the shape principal components. All of these approaches are deterministic and therefore unable to estimate how image quality will manifest in shape uncertainty. In this paper, we determine the LA shape as the shape that maximises the posterior conditional probability. This allows us to quantify uncertainties such as image artefacts and to quantify the level of uncertainty affecting the anatomy. Bayesian Convolutional neural networks (BCNN) have been proposed as a potential solution to avoid the over-fitting affecting CNN when the training set is small (Srivastava et al. (2014); Peretroukhin et al. (2017)); BCNN treats network weights as a probability distribution rather than as deterministic numbers allowing the network to provide an uncertainty estimate. Whereas this approach quantifies uncertainty, it presents some limitations that make it inadequate for the purposes presented in this paper. First, BCNN provides the probability a voxel is/is not myocardial tissue, hence the granularity is restricted by the voxel size. Second, BCNN quantifies the uncertainty by sampling the network parameters, then forward propagating the image on each sampled CNN and finally using a Monte Carlo (MC) approach. CNN used in

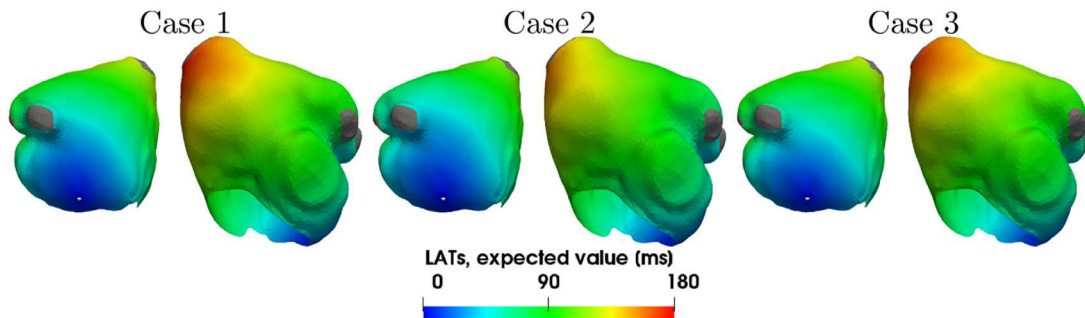


Fig. 11. Expected LAT for cases 1,2,3. The grey sphere represents the activation starting point.

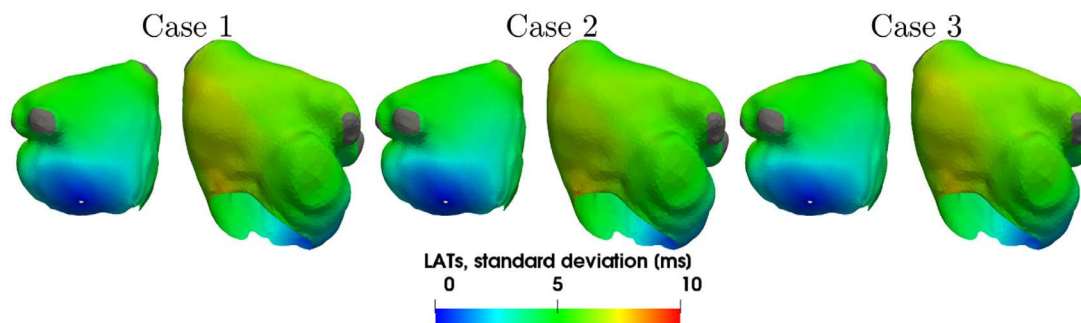


Fig. 12. Distribution of the standard deviation on LAT for cases 1,2,3. The grey sphere represents the activation starting point.

atrial segmentation are characterised by a large number of weights (Xiong et al. (2019); de Vente et al. (2019)): hence, MC may require a large number of samples to adequately represent the output uncertainty. Conversely, the approach we proposed in this paper provides a closed form for the probability distribution of the LA shape and achieves a higher sampling efficiency.

**Error magnitude** In this paper, we obtained MRI with the resolution of (0.94 mm, 0.94 mm, 2 mm), as reported in Section 2.1. When describing the shape with 15 modes, the cross-validation test on the truncation error (Section 3.3) showed a standard deviation of 1.96 mm ( $CI_{95} = 2.74$  mm): this value is comparable with the image resolution. However, when we consider the truncation error as a 3D vector field, the vector magnitude of the mean of the truncation error does not exceed 0.15 mm (Fig. 4 - B), a value negligible if compared with the MRI resolution.

Discrepancies between measured and computed anatomies (Section 3.6) presented a standard deviation of 2.34 mm ( $CI_{95} = 4.58$  mm). This value has the same order of magnitude as the image resolution; however, it performs better than the mean shape (standard deviation 3.51 mm,  $CI_{95} = 6.88$  mm). The performances are affected by the uncertainty model, since the parameters were set using the training set. Discrepancies evaluated between measured anatomies and computed anatomies either in absence or in presence of an uncertainty along the z (slice) directions (Section 3.6) showed standard deviations of 2.55 mm and 2.83 mm and hence demonstrate the robustness of the model.

**Uncertainty on simulations** Stochastic collocation techniques, (Castrillón-Candás et al., 2016; Sankaran and Marsden, 2011) are widely used to determine the uncertainty on a computed solution when the uncertainty affects the computational domain. The approach we presented is compatible with stochastic collocation techniques efficiently, as i) the principal directions capture the largest variability (in the statistical sense) using a smaller number of parameters ii) the principal components are mutually independent and ordered: adding new components allows refinement of the representation of the anatomy. The uncertainty on local activation times evaluated in Section 3.7 is a cumulative function that increases in late-activated regions. In the 3 cases we tested in Section 3.7, we found a maximum standard deviation on LATs of ~ 8ms: this value is comparable with the LATs stability of 4ms used in Roney et al. (2019a).

**Applications of the proposed approach** Personalised computational models represent a novel framework for understanding the mechanisms that develop and sustain atrial fibrillation and for tailoring and optimising the treatment. Recent works (Prakosa et al. (2018); Boyle et al. (2019)) propose to identify the optimal ablation target from cardiac clinical imaging and computational models and then register this on the electroanatomical mapping anatomy to inform the clinician. Quantifying the model uncertainty and its impact on the identification of the ablation outcome adds robustness to the process. The framework we propose in this

study supports this goal, as it allows the quantification of the uncertainty on the numerical simulation output and the registration process. This increases the robustness of the entire process. Specifically, we showed that uncertainties in the atrial anatomy affect the predicted activation maps.

## 5. Limitations

Anatomies are evaluated from image segmentation, that is a semi-automated process; hence, this introduces uncertainty, as far as inter-operator variability is concerned. We have taken the segmented images as a ground truth, however, multiple segmentations by the same or different operators would have provided a consensus and potentially better estimate of the underlying atrial shape.

The technique presented here requires that anatomies are described with a Delaunay triangulation with a fixed number of points. This implies registering an atlas on measured anatomy. Hence, the registration process introduces uncertainty, especially in regions where the discrepancy between the deformed atlas and the measured anatomy is large. In this paper, we did not take into account this source of uncertainty. However, upon visual inspection we found no significant discrepancies.

Overall, the process requires some manual steps, such as the segmentation and the alignment (rigid registration) between the atlas and the measured surface before registration; this poses a limit on scaling this current approach to very large data sets.

The left atrium is a 3D structure, and varying thickness across the wall will potentially influence activation patterns (Song et al. (2017)). In the current study, we focused on 2D shell models as the left atrial anatomy was obtained using MRI images with a resolution of  $0.94 \times 0.94 \times 2$  mm<sup>3</sup>, this is insufficient to measure the thin atrial wall, which can be < 1 mm (Whitaker et al. (2017)). To capture the complex 3D atrial anatomy, models could be constructed from CT images, (Fastl et al., 2018). The proposed method could be applied to these meshes by either treating the endocardial and epicardial as two shell meshes or treating the model as a closed surface. With either approach, it is possible to represent the 3D anatomy by a 2D surface that can be processed by our proposed method. However, this may require the addition of more modes to sufficiently capture both the endocardial and epicardial shape.

In Section 3.7 we modelled the left atrium with a 2D isotropic model. This choice reflects the complexity of the clinical data available as clinicians typically have access to the endocardial surface only during EP investigation. While fibre orientation can impact for local activation patterns (Fastl et al. (2018)) and fibrillation simulations (Roney et al. (2019b)), we have previously shown that we can create and validate models of atrial paced activation from clinical data using isotropic models that reflect the resolution of clinical data available (Corrado et al. (2018a)). When we evaluated the

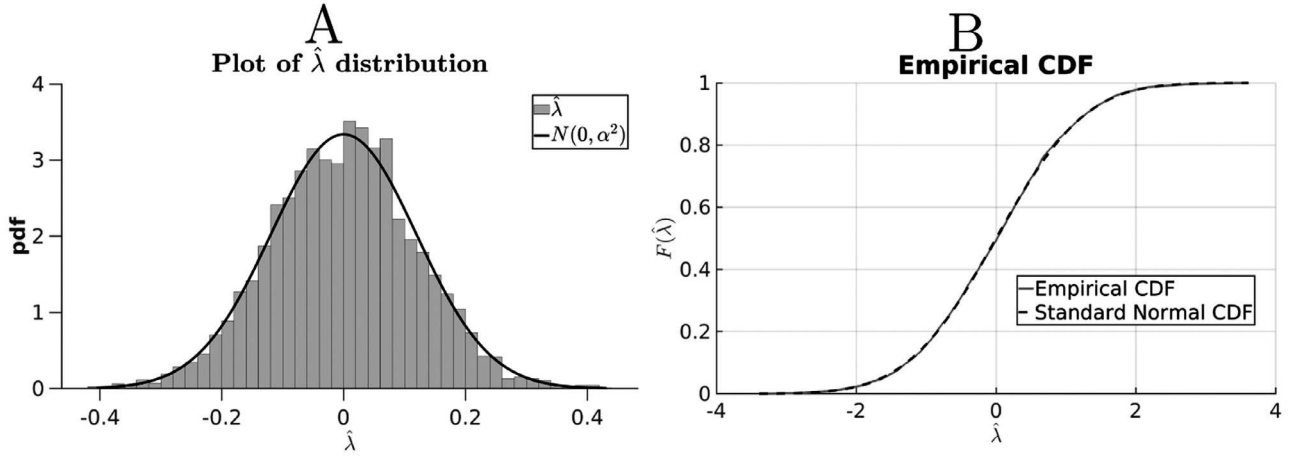


**Fig. A.13.** A: Histogram plot of the distribution of  $\hat{\lambda}$ ; the black line represents the normal distribution  $N(0, \alpha^2)$ . B: QQ plot of the empirical cumulative density function (cdf) and the standard normal cdf.

statistics of the local activation times in Section 3.7, we identified the source point for the eikonal model as a mesh point in the proximity of the coronary sinus. Then we adopted the same point as the source for each sample. Being a mesh point, the source will move, introducing uncertainty. In the present work, however, we did not take into account this source of uncertainty.

Eq. (7) describes the covariance model for the uncertainty. This model is isotropic and depends on 2 parameters that have been evaluated using a maximum joint posterior estimation algorithm on the training set. Hence, the error model does not take into account the effects of anisotropic resolution on the MRI images. While the anisotropic orientation is constant if referred to the MRI reference frame, factors including anatomical variability between individuals and patient position within the MRI scanner lead to a directional distribution of the anisotropy. This represents an additional error source that could be included in the error model but would require another term in the error model and further optimisation. Strong artefacts, scanner type, modality of the image sequence, breath artefacts ... are all factors that affect the error model. The error model chosen and determined on a training set might not well represent some cases.

## 6. Conclusions

We have developed a method to sample from an anatomy probability distribution and to infer model uncertainty. We implemented a PCA decomposition for the anatomy, obtaining a method that is computationally efficient.

### Declaration of Competing Interest

We wish to confirm that there are no known conflicts of interest associated with this publication and there has been no significant financial support for this work that could have influenced its outcome.

### Acknowledgements

This work was supported by the EPSRC (EP/P101268X/1), the Wellcome centre and the Department of Health via the National Institute for Health Research (NIHR) comprehensive Biomedical Research Centre award to Guy's & St Thomas' NHS Foundation Trust in partnership with King's College London and King's College Hospital NHS Foundation Trust.

## Appendix A. An equivalent representation for $\hat{\lambda}$

In Corrado et al. (2018b) we represented the distribution  $\lambda^* \simeq N(0, \Sigma_\lambda)$  with  $\Sigma_\lambda = \Theta^T \alpha^2 \Theta$ ,  $\alpha$  being a positive scalar value. Next, we proved the existence of variables  $\hat{\lambda} \sim N(\mathbf{0}, \alpha^2 I)$ , such that  $\lambda \Theta \hat{\lambda}$ .

Following the same procedure presented in Section 2.5, we first evaluate:

$$\hat{\lambda}^i = \Theta^{-1} U^T (\mathbf{X}_{\text{obs}}^i - \boldsymbol{\mu}), \quad i = 1 \dots M$$

If the null hypothesis holds,  $\hat{\lambda}_j^i, i = 1 \dots M, j = 1 \dots N_{\text{modes}}$  represent  $N_{\text{modes}} \times M$  realisations of  $N(0, \alpha^2)$  Approximating  $\alpha^2$  with the sampling covariance,  $s^2$ , we have:

$$s^2 = \frac{1}{(N_{\text{modes}} \times M) - 1} \sum_{i=1}^M \sum_{j=1}^{N_{\text{modes}}} (\hat{\lambda}_j^i - \mu_{\hat{\lambda}})^2,$$

$$\mu_{\hat{\lambda}} = \frac{1}{(N_{\text{modes}} \times M)} \sum_{i=1}^M \sum_{j=1}^{N_{\text{modes}}} \hat{\lambda}_j^i$$

Using the training set samples, we evaluated the sample mean and the sample standard deviation giving  $\mu_{\hat{\lambda}} \approx 1e^{-17}$  and  $\alpha \approx 0.12$ , while the Kolmogorov Smirnov test found no evidence to reject the null hypothesis ( $p=0.44$ ). The histogram plot (Fig. A.13 -A) and the QQ plot (Fig. A.13 -B) for  $\hat{\lambda}$  showed excellent agreement with a standard normal distribution.

## Appendix B. Reduced rank approximation of $\Sigma_{\mathbf{e}_{\text{TOT}}}$

The covariance matrix  $\Sigma_{\mathbf{e}_{\text{TOT}}}$  is a 3 blocks block-diagonal matrix, as defined in (7). Each block  $B$  consists of a dense ill-conditioned matrix with rank  $r_0 = 13569$  and condition number ranging between  $0.410^9$  (10 modes) and  $4.210^9$  (69 modes).

Computing  $\boldsymbol{\mu}_{\text{post}}$  and  $\Sigma_{\lambda, \text{post}}$  defined in (8) requires inverting  $B$ : this amplifies the numerical errors.

In this paper, we adopted a reduced rank (RR) representation for  $B$ , using the Matlab function *decompose* with a complete orthogonal decomposition (COD) and setting a rank tolerance of 0.1. We have chosen this threshold proceeding as follows. First, we applied the QR decomposition to  $B$ . Next, we evaluated the largest absolute value  $R_{\text{max}}$  of the diagonal entries of  $R$ . Finally, we set the threshold to a value equal to 0.01% of  $R_{\text{max}}$ .

Fig. B.14 shows the absolute values of the diagonal entries of  $R$  for different choices of the number of modes. This approach

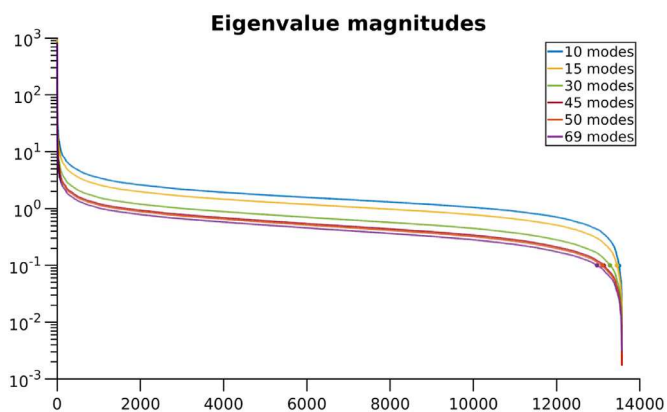


**Fig. B.14.** Plot of the absolute values of the diagonal entries of matrix  $R$  for different choices of the number of modes. Markers represent the first element with a threshold below 0.1.

removed the part of the spectrum delimited by the markers. All the markers are located in the proximity of the fast decaying of the spectrum. Overall, this approach removed 1.7 – 11.3% (rank: 12305–13337) of the lowest matrix spectrum.

## References

- Beg, M.F., Miller, M.I., Trounev, A., Younes, L., 2005. Computing large deformation metric mappings via geodesic flows of diffeomorphisms. *Int. J. Comput. Vision* 61 (2), 139–157. doi:[10.1023/B:VISI.0000043755.93987.a](https://doi.org/10.1023/B:VISI.0000043755.93987.a).
- Biegling, E.T., Morris, A., Wilson, B.D., McGann, C.J., Marrouche, N.F., Cates, J., 2018. Left atrial shape predicts recurrence after atrial fibrillation catheter ablation. *J. Cardiovasc. Electrophysiol.* 29 (7), 966–972. doi:[10.1111/jce.13641](https://doi.org/10.1111/jce.13641).
- Boyle, P.M., Zghaib, T., Zahid, S., Ali, R.L., Deng, D., Franceschi, W.H., Hakim, J.B., Murphy, M.J., Prakosa, A., Zimmerman, S.L., Ashikaga, H., Marine, J.E., Kolandaivelu, A., Nazarian, S., Spragg, D.D., Calkins, H., Trayanova, N.A., 2019. Computationally guided personalized targeted ablation of persistent atrial fibrillation. *Nat. Biomed. Eng.* doi:[10.1038/s41551-019-0437-9](https://doi.org/10.1038/s41551-019-0437-9).
- Carpenter, B., Gelman, A., Hoffman, M., Lee, D., Goodrich, B., Betancourt, M., Brubaker, M., Guo, J., Li, P., Riddell, A., 2017. Stan: a probabilistic programming language. *J. Stat. Softw. Articles* 76 (1), 1–32. doi:[10.18637/jss.v076.i01](https://doi.org/10.18637/jss.v076.i01).
- Castrillón-Candás, J., Nobile, F., Tempone, R., 2016. Analytic regularity and collocation approximation for elliptic pdes with random domain deformations. *Comput. Math. Appl.* 71 (6), 1173–1197. doi:[10.1016/j.camwa.2016.01.005](https://doi.org/10.1016/j.camwa.2016.01.005).
- Colli Franzese, P., Pavarino, L.F., Savaré, G., 2006. Computational electrocardiology: mathematical and numerical modeling. In: Quarteroni, A., Formaggia, L., Veneziani, A. (Eds.), *Complex Systems in Biomedicine*. Springer Milan, Milano, pp. 187–241. doi:[10.1007/88-470-0396-2\\_6](https://doi.org/10.1007/88-470-0396-2_6).
- Corrado, C., Niederer, S.A., 2016. A two-variable model robust to pacemaker behaviour for the dynamics of the cardiac action potential. *Math. Biosci.* 281, 46–54. doi:[10.1016/j.mbs.2016.08.010](https://doi.org/10.1016/j.mbs.2016.08.010).
- Corrado, C., Whitaker, J., Chubb, H., Williams, S., Wright, M., Gill, J., O'Neill, M., Niederer, S., 2016. Predicting spiral wave stability by personalized electrophysiology models. In: 2016 Computing in Cardiology Conference (CinC), pp. 229–232. doi:[10.23919/CIC.2016.7868721](https://doi.org/10.23919/CIC.2016.7868721).
- Corrado, C., Whitaker, J., Chubb, H., Williams, S., Wright, M., Gill, J., O'Neill, M.D., Niederer, S.A., 2017. Personalized models of human atrial electrophysiology derived from endocardial electrograms. *IEEE Trans. Biomed. Eng.* 64 (4), 735–742.
- Corrado, C., Williams, S., Karim, R., Plank, G., O'Neill, M., Niederer, S., 2018. A work flow to build and validate patient specific left atrium electrophysiology models from catheter measurements. *Med. Image Anal.* 47, 153–163. doi:[10.1016/j.media.2018.04.005](https://doi.org/10.1016/j.media.2018.04.005).
- Corrado, C., Williams, S., Sim, I., Coveney, S., O'Neill, M., Wilkinson, R., Oakley, J., Clayton, R., Niederer, S., 2018. An algorithm to sample an anatomy with uncertainty. *Comput. Cardiol.* 45, 1–4. doi:[10.22489/CinC.2018.078](https://doi.org/10.22489/CinC.2018.078).
- Corrado, C., Zemzemi, N., 2018. A conduction velocity adapted eikonal model for electrophysiology problems with re-excitability evaluation. *Med. Image Anal.* 43, 186–197. doi:[10.1016/j.media.2017.11.002](https://doi.org/10.1016/j.media.2017.11.002).
- Dhamala, J., Arevalo, H.J., Sapp, J., Horcek, B.M., Wu, K.C., Trayanova, N.A., Wang, L., 2018. Quantifying the uncertainty in model parameters using gaussian process-based markov chain monte carlo in cardiac electrophysiology. *Med. Image Anal.* 48, 43–57. doi:[10.1016/j.media.2018.05.007](https://doi.org/10.1016/j.media.2018.05.007).
- Durleman, S., Prastawa, M., Charon, N., Korenberg, J.R., Joshi, S., Gerig, G., Trounev, A., 2014. Morphometry of anatomical shape complexes with dense deformations and sparse parameters. *NeuroImage* 101, 35–49. doi:[10.1016/j.neuroimage.2014.06.043](https://doi.org/10.1016/j.neuroimage.2014.06.043).
- Fastl, T.E., Tobon-Gomez, C., Crozier, A., Whitaker, J., Rajani, R., McCarthy, K.P., Sanchez-Quintana, D., Ho, S.Y., O'Neill, M.D., Plank, G., Bishop, M.J., Niederer, S.A., 2018. Personalized computational modeling of left atrial geometry and transmural myofiber architecture. *Med. Image Anal.* 47, 180–190. doi:[10.1016/j.media.2018.04.001](https://doi.org/10.1016/j.media.2018.04.001).
- Gray, R.A., Pathmanathan, P., 2018. Patient-specific cardiovascular computational modeling: diversity of personalization and challenges. *J. Cardiovasc. Transl. Res.* 11 (2), 80–88. doi:[10.1007/s12265-018-9792-2](https://doi.org/10.1007/s12265-018-9792-2).
- MIRTK. <https://biomedica.doc.ic.ac.uk/software/mirtk/>.
- Hotelling, H., 1933. Analysis of a complex of statistical variables with principal components. *J. Educ. Psychol.* 24, 417–441.
- Johnston, B.M., Coveney, S., Chang, E.T.Y., Johnston, P.R., Clayton, R.H., 2018. Quantifying the effect of uncertainty in input parameters in a simplified bidomain model of partial thickness ischaemia. *Med. Biol. Eng. Comput.* 56 (5), 761–780. doi:[10.1007/s11517-017-1714-y](https://doi.org/10.1007/s11517-017-1714-y).
- Lewandowski, A.J., Augustine, D., Lamata, P., Davis, E.F., Lazdam, M., Francis, J., McCormick, K., Wilkinson, A.R., Singhal, A., Lucas, A., Smith, N.P., Neubauer, S., Leeson, P., 2013. Preterm heart in adult life. *Circulation* 127 (2), 197–206. doi:[10.1161/CIRCULATIONAHA.112.126920](https://doi.org/10.1161/CIRCULATIONAHA.112.126920).
- Minasny, B., McBratney, A.B., 2005. The matern function as a general model for soil variograms. *Geoderma* 128 (3), 192–207. doi:[10.1016/j.geoderma.2005.04.003](https://doi.org/10.1016/j.geoderma.2005.04.003).
- Mirams, G.R., Pathmanathan, P., Gray, R.A., Challenor, P., Clayton, R.H., 2016. Uncertainty and variability in computational and mathematical models of cardiac physiology. *J. Physiol.* 594 (23), 6833–6847. doi:[10.1113/jp271671](https://doi.org/10.1113/jp271671).
- Niederer, S.A., Campbell, K.S., Campbell, S.G., 2019. A short history of the development of mathematical models of cardiac mechanics. *J. Mol. Cellular Cardiol.* 127, 11–19. doi:[10.1016/j.yjmcc.2018.11.015](https://doi.org/10.1016/j.yjmcc.2018.11.015).
- Peretroukhin, V., Clement, L., Kelly, J., 2017. Reducing drift in visual odometry by inferring sun direction using a bayesian convolutional neural network. In: 2017 IEEE International Conference on Robotics and Automation (ICRA), pp. 2035–2042. doi:[10.1109/ICRA.2017.7989235](https://doi.org/10.1109/ICRA.2017.7989235).
- Prakosa, A., Arevalo, H.J., Deng, D., Boyle, P.M., Nikolov, P.P., Ashikaga, H., Blauer, J.J.E., Ghafoori, E., Park, C.J., Blake, R.C., Han, F.T., MacLeod, R.S., Halperin, H.R., Callans, D.J., Ranjan, R., Chrispin, J., Nazarian, S., Trayanova, N.A., 2018. Personalized virtual-heart technology for guiding the ablation of infarct-related ventricular tachycardia. *Nat. Biomed. Eng.* 2 (10), 732–740. doi:[10.1038/s41551-018-0282-2](https://doi.org/10.1038/s41551-018-0282-2).
- Quaglino, A., Pezzuto, S., Koutsourelakis, P.S., Auricchio, A., Krause, R., 2018. Fast uncertainty quantification of activation sequences in patient-specific cardiac electrophysiology meeting clinical time constraints. *Int. J. Numer. Methods Biomed. Eng.* 34 (7), e2985. doi:[10.1002/cnm.2985](https://doi.org/10.1002/cnm.2985).
- Razeghi, O., Karim, R., Whitaker, J., Tobon-Gomez, C., Niederer, S., 2017. A platform for quantifying atrial structural remodeling. *Comput. Cardiol.* 44, 1–4. doi:[10.22489/CinC.2017.047-306](https://doi.org/10.22489/CinC.2017.047-306).
- Roney, C.H., Whitaker, J., Sim, I., O'Neill, L., Mukherjee, R.K., Razeghi, O., Vigmond, E.J., Wright, M., O'Neill, M.D., Williams, S.E., Niederer, S.A., 2019. A technique for measuring anisotropy in atrial conduction to estimate conduction velocity and atrial fibre direction. *Comput. Biol. Med.* 104, 278–290. doi:[10.1016/j.combiomed.2018.10.019](https://doi.org/10.1016/j.combiomed.2018.10.019).
- Roney, C.H., Whitaker, J., Sim, I., O'Neill, L., Mukherjee, R.K., Razeghi, O., Vigmond, E.J., Wright, M., O'Neill, M.D., Williams, S.E., et al., 2019. A technique for measuring anisotropy in atrial conduction to estimate conduction velocity and atrial fibre direction. *Comput. Biol. Med.* 104, 278–290.
- Roney, C.H., Williams, S.E., Cochet, H., Mukherjee, R.K., O'Neill, L., Sim, I., Whitaker, J., Razeghi, O., Klein, G.J., Vigmond, E.J., O'Neill, M., Niederer, S.A., 2018. Patient-specific simulations predict efficacy of ablation of interatrial connections for treatment of persistent atrial fibrillation. *EP Europace* 20 (suppl\_3), iii55–iii68.
- Sankaran, S., Marsden, A., 2011. A stochastic collocation method for uncertainty quantification and propagation in cardiovascular simulations. *ASME J. Biomech. Eng.* 133 (3), 031001–031001–12. doi:[10.1115/1.4003259](https://doi.org/10.1115/1.4003259).
- Song, J.-S., Wi, J., Lee, H.-J., Hwang, M., Lim, B., Kim, T.-H., Uhm, J., Jang, B., Lee, M., Seo, J.-W., Pak, H.-N., 2017. Role of atrial wall thickness in wave-dynamics of atrial fibrillation. *PLOS ONE* 12 (8), 1–12. doi:[10.1371/journal.pone.0182174](https://doi.org/10.1371/journal.pone.0182174).
- Srivastava, N., Hinton, G., Krizhevsky, A., Sutskever, I., Salakhutdinov, R., 2014. Dropout: a simple way to prevent neural networks from overfitting. *J. Mach. Learn. Res.* 15, 1929–1958.
- Stone, M., 1974. Cross-validatory choice and assessment of statistical predictions. *J. R. Stat. Soc. Series B* 36 (2), 111–147.
- Varela, M., Bisbal, F., Zacur, E., Berrueto, A., Aslanidi, O.V., Mont, L., Lamata, P., 2017. Novel computational analysis of left atrial anatomy improves prediction of atrial fibrillation recurrence after ablation. *Front. Physiol.* 8, 68.
- de Vente, C., Veta, M., Razeghi, O., Niederer, S., Pluim, J., Rhode, K., Karim, R., 2019. Convolutional neural networks for segmentation of the left atrium from gadolinium-enhancement mri images. In: Pop, M., Sermesant, M., Zhao, J., Li, S., McLeod, K., Young, A., Rhode, K., Mansi, T. (Eds.), *Statistical Atlases and Computational Models of the Heart. Atrial Segmentation and LV Quantification Challenges*. Springer International Publishing, Cham, pp. 348–356.
- Whitaker, J., Panikker, S., Fastl, T., Corrado, C., Virmani, R., Kutys, R., Lim, E., O'Neill, M., Nicol, E., Niederer, S., Wong, T., 2017. Cardiac ct assessment of tissue thickness at the ostium of the left atrial appendage predicts acute success of radiofrequency ablation. *Pacing Clin. Electrophysiol.* 40 (11), 1218–1226. doi:[10.1111/pace.13203](https://doi.org/10.1111/pace.13203).
- Xiong, Z., Fedorov, V.V., Fu, X., Cheng, E., Macleod, R., Zhao, J., 2019. Fully automatic left atrium segmentation from late gadolinium enhanced magnetic resonance imaging using a dual fully convolutional neural network. *IEEE Trans. Med. Imag.* 38 (2), 515–524.